



**HAL**  
open science

## Multiple Early Eocene carbon isotope excursions associated with environmental changes in the Dieppe-Hampshire Basin (NW Europe)

Sylvain Garel, Christian Dupuis, Florence Quesnel, Jérémy Jacob, Johan Yans, Roberto Magioncalda, Christine Fléhoc, Johann Schnyder

► **To cite this version:**

Sylvain Garel, Christian Dupuis, Florence Quesnel, Jérémy Jacob, Johan Yans, et al.. Multiple Early Eocene carbon isotope excursions associated with environmental changes in the Dieppe-Hampshire Basin (NW Europe). *Bulletin de la Société Géologique de France*, 2020, 10.1051/bsgf/2020030 . hal-02950486v1

**HAL Id: hal-02950486**

**<https://hal.science/hal-02950486v1>**

Submitted on 28 Sep 2020 (v1), last revised 18 Nov 2020 (v2)

**HAL** is a multi-disciplinary open access archive for the deposit and dissemination of scientific research documents, whether they are published or not. The documents may come from teaching and research institutions in France or abroad, or from public or private research centers.

L'archive ouverte pluridisciplinaire **HAL**, est destinée au dépôt et à la diffusion de documents scientifiques de niveau recherche, publiés ou non, émanant des établissements d'enseignement et de recherche français ou étrangers, des laboratoires publics ou privés.

1 Multiple early Eocene carbon isotope excursions associated with  
2 environmental changes in the Dieppe-Hampshire Basin (NW Europe)

3 Multiples excursions isotopiques du carbone de l'Eocène inférieur  
4 associées à des changements environnementaux dans le Bassin de  
5 Dieppe-Hampshire (Europe du NO)

6 Authors: Sylvain GAREL <sup>a,b,c,\*</sup>, Christian DUPUIS <sup>d</sup>, Florence QUESNEL <sup>b,c</sup>, Jérémy JACOB <sup>b,e</sup>, Johan  
7 YANS <sup>f</sup>, Roberto MAGIONCALDA <sup>g</sup>, Christine FLÉHOC <sup>h</sup> and Johann SCHNYDER <sup>a</sup>

8 <sup>a</sup> Sorbonne Université, CNRS-INSU, IStEP UMR 7193, 4 Place Jussieu, 75005 Paris, France

9 <sup>b</sup> Université d'Orléans, CNRS, BRGM, Institut des Sciences de la Terre d'Orléans (ISTO), UMR  
10 7327, 45071 Orléans, France

11 <sup>c</sup> BRGM GéoRessources/GAT, 45060 Orléans Cedex 2, France

12 <sup>d</sup> Laboratoire de Géologie Fondamentale et Appliquée, Faculté Polytechnique de Mons, Université de Mons, rue  
13 de Houdain 9, B-7000 Mons, Belgium

14 <sup>e</sup> Laboratoire des Sciences du Climat et de l'Environnement, CEA-CNRS-UVSQ, Université Paris-Saclay,  
15 91198, Gif-sur-Yvette, France

16 <sup>f</sup> University of Namur, Department of Geology, Institute of Life, Earth and Environment, ILEE, 61 rue de  
17 Bruxelles, 5000 Namur, Belgium

18 <sup>g</sup> FRAMATOME, HPC Project, 1 Place Jean Miller, 92400 Courbevoie, France

19 <sup>h</sup> BRGM Direction des Laboratoires/ISO, 45060 Orléans Cedex 2, France

20

21

22

23

24

25

26

27

28

29

30

31 \* Corresponding author: [sylvain.garel.laurin@gmail.com](mailto:sylvain.garel.laurin@gmail.com)

32 **Keywords:** early Eocene, carbon isotope excursions, PETM, paleohydrology, palynofacies, Dieppe-  
33 Hampshire Basin

34 **Mots-clés :** Eocène inférieur, excursions isotopiques du carbone, PETM, paléohydrologie,  
35 palynofaciès, Bassin de Dieppe-Hampshire

36 ABSTRACT

37 The early Eocene experienced a series of short-lived global warming events, known as hyperthermals,  
38 associated with negative carbon isotope excursions (CIE). The Paleocene-Eocene Thermal Maximum  
39 (PETM or ETM-1) and Eocene Thermal Maximum 2 (ETM-2) are the two main events of this Epoch,  
40 both marked by massive sea-floor carbonate dissolution. Their timing, amplitude and impacts are  
41 rather well documented, but CIEs with lower amplitudes also associated with carbonate dissolution are  
42 still poorly studied (e.g. events E1 to H1), especially in the terrestrial realm where  
43 hiatus/disconformities and various sedimentary rates in a single succession may complicate the  
44 assignment to global isotopic events.

45 Here we present a new high-resolution multi-proxy study on the terrestrial, lagoonal and shallow  
46 marine late Paleocene-early Eocene succession from two sites of the Cap d'Ailly area in the Dieppe-  
47 Hampshire Basin (Normandy, France). Carbon isotope data ( $\delta^{13}\text{C}$ ) on bulk organic matter and higher-  
48 plant derived *n*-alkanes, and K-Ar ages on authigenic glauconite were determined to provide a  
49 stratigraphic framework. Palynofacies, distribution and hydrogen isotope values ( $\delta^2\text{H}$ ) of higher-plant  
50 derived *n*-alkanes allowed us to unravel paleoenvironmental and paleoclimatic changes. In coastal  
51 sediments of the Cap d'Ailly area,  $\delta^{13}\text{C}$  values revealed two main negative CIEs, from base to top  
52 CIE1 and CIE2, and 3 less pronounced negative excursions older than the NP11 nanofossil biozone.  
53 While the CIE1 is clearly linked with the PETM initiation, the CIE2 could either correspond to 1) a  
54 second excursion within the PETM interval caused by strong local environmental changes or 2) a  
55 global carbon isotopic event that occurred between the PETM and ETM-2.

56 Paleoenvironmental data indicated that both main CIEs were associated with dramatic changes such as  
57 eutrophication, algal and/or dinoflagellate blooms along with paleohydrological variations and an

58 increase in seasonality. They revealed that the intervals immediately below these CIEs are also marked  
59 by environmental and climatic changes. Thus, this study shows either 1) a PETM marked by at least  
60 two distinct intervals of strong environmental and climatic changes or 2) at least one “minor” CIE: E1,  
61 E2, F or G, was associated with strong environmental and climatic changes similar to those that  
62 occurred during the PETM.

### 63 RESUME

64 L’Eocène inférieur fût le théâtre d’une série de réchauffements climatiques rapides et globaux nommés  
65 hyperthermaux qui sont associés à des excursions isotopiques négatives du carbone (CIE = *Carbon*  
66 *Isotope Excursion*). Le maximum thermique du Paléocène-Eocène (PETM = *Paleocene-Eocene*  
67 *Thermal Maximum* ou ETM-1 = *Eocene Thermal Maximum-1*) et le Maximum Thermique de  
68 l’Eocène-2 (ETM-2) sont les deux évènements principaux de cette Epoque et sont tous les deux  
69 marqués par la dissolution massive de carbonates des fonds marins. Leurs timings, amplitudes et  
70 impacts sont plutôt bien documentés, mais des CIEs de plus faible amplitude, également associées à  
71 des dissolutions de carbonates, sont encore peu étudiées (p. ex. évènements E1 à H1), notamment dans  
72 le domaine continental où les hiatus/inconformités ainsi que les taux de sédimentation variables dans  
73 une même succession compliquent l’identification des évènements isotopiques globaux.

74 Ici, nous présentons une nouvelle étude ‘multi-proxy’ à haute résolution sur la succession continentale,  
75 lagunaire et marine peu profonde de deux sites du secteur du Cap d’Ailly dans le Bassin de Dieppe-  
76 Hampshire (Normandie). Les données isotopiques du carbone ( $\delta^{13}\text{C}$ ) de la matière organique totale et  
77 des *n*-alcanes de végétaux supérieurs ainsi que les âges K-Ar de glauconies authigènes ont été  
78 déterminés pour obtenir un cadre stratigraphique robuste. Les palynofaciès ainsi que la distribution et  
79 les données isotopiques de l’hydrogène ( $\delta^2\text{H}$ ) de *n*-alcanes de végétaux supérieurs nous ont permis de  
80 reconstituer les changements paléoenvironnementaux et paléoclimatiques survenus durant l’intervalle  
81 étudié. Dans les sédiments côtiers du secteur du Cap d’Ailly, les courbes de  $\delta^{13}\text{C}$  montrent 2  
82 principales CIEs négatives, de la base au sommet : CIE1 et CIE2, et 3 excursions négatives moins  
83 prononcées, toutes plus anciennes que la biozone à nannofossiles NP11. Alors que la CIE1 est  
84 clairement liée à l’initiation du PETM, la CIE2 pourrait correspondre, soit 1) à une seconde excursion

85 au sein du PETM causée par un important changement environnemental local, soit 2) à un évènement  
86 isotopique du carbone global qui ce serait produit entre le PETM et l'ETM-2.

87 Les données paléoenvironnementales indiquent que les deux principales CIEs sont associées à des  
88 changements importants comme l'eutrophisation, des proliférations d'algues et/ou de dinoflagellés  
89 associés à des variations paléohydrologiques et à une augmentation de la saisonnalité. Elles révèlent  
90 que les intervalles immédiatement sous les CIEs sont aussi marqués par des changements  
91 environnementaux et climatiques. Ainsi, cette étude montre que : soit 1) le PETM fut marqué par au  
92 moins deux intervalles distincts de forts changements environnementaux et climatiques, ou 2) qu'au  
93 moins une CIE mineure : E1, E2, F ou G fut associée à des changements environnementaux et  
94 climatiques similaires à ceux qui se sont produits pendant le PETM.

## 95 1. Introduction

96 The late Paleocene and early Eocene were marked by a series of extreme and fast transient global  
97 hyperthermal events (Coccioni et al., 2012; Cramer et al., 2003; Lourens et al., 2005; Westerhold et  
98 al., 2018). During these events, global average temperatures eventually rose by as much as 7°C above  
99 pre-hyperthermal ones (Krishnan et al., 2014; McInerney and Wing, 2011). The hyperthermals are all  
100 characterized by carbonate dissolution horizons in marine successions and negative carbon isotope  
101 excursions (CIE) linked to the release of a large amount of isotopically depleted carbon in the ocean-  
102 atmosphere system (Littler et al., 2014; Lourens et al., 2005; Zachos et al., 2005). The largest  
103 hyperthermal, the Paleocene-Eocene Thermal Maximum (PETM or ETM-1), occurred around 56 Ma  
104 (Westerhold et al., 2017) and was associated with benthic foraminifera extinction in oceans (Kennett  
105 and Stott, 1991) and the appearance and rapid dispersal of modern mammalian orders on land (Smith  
106 et al., 2006). Other well-known warming events such as ETM-2 (or ELMO; ~54 Ma) and ETM-3 (or  
107 “X” event; ~52.8 Ma) occurred during the early Eocene (Lauretano et al., 2015; Westerhold et al.,  
108 2017). They had a smaller impact on climate and on the terrestrial fauna (Abels et al., 2016; Noiret et  
109 al., 2016).

110 Cramer et al. (2003) showed that four events, “E1”, “E2”, “F” and “G”, still poorly studied, occurred  
111 between PETM and ETM-2, respectively 250, 350, 750 and 940 ka after the PETM (Westerhold et al.,  
112 2017). Their CIE magnitudes are much smaller than that of the PETM, even though the “E1” CIE  
113 magnitude can reach half of that of the PETM in Italy (Coccioni et al., 2012). These events are  
114 associated to a decrease in  $\delta^{18}\text{O}$  values and in carbonate content (Coccioni et al., 2012), but their  
115 climatic and environmental impacts have never been discussed in detail, especially on land.

116 In France, Upper Paleocene and Lower Eocene terrestrial and lagoonal sediments corresponding to the  
117 regional “Sparnacian” stage are known to record the PETM and are found in the Corbieres (South of  
118 France, Yans et al., 2014), Paris and Dieppe-Hampshire basins among others (Aubry et al., 2005). In  
119 the Dieppe-Hampshire Basin, these Sparnacian facies are well exposed to the west of Dieppe  
120 (Normandy; Fig. 1) with a maximum thickness of 15 m in the Cap d’Ailly area. The coastal swamp  
121 sediments of this area record the PETM and dramatic environmental changes in the lower lignite

122 complex (L1) of the Mortemer Formation representing only a fraction of the Sparnacian succession  
123 (Garel et al., 2013; Magioncalda et al., 2001; Storme et al., 2012).

124 Here we present a multi-proxy study of the Phare d'Ailly core that displays almost the whole local  
125 Sparnacian sedimentary succession. Compound-specific  $\delta^{13}\text{C}$  values and K-Ar ages on authigenic  
126 glauconite were determined and compared to micropaleontology and palynology records to build a  
127 stratigraphic framework and unravel CIEs. Palynofacies and relative abundances and distributions of  
128 *n*-alkanes provided clues about vegetation succession and other environmental changes.  
129 Paleohydrological changes were constrained by  $\delta^2\text{H}$  values of *n*-alkanes. Our integrated data unravel  
130 climatic and environmental changes at other time intervals than the one occurring at the Paleocene-  
131 Eocene boundary and their possible link with carbon isotopic events in this mid-latitude coastal  
132 environment.

## 133 2. Sample locations and methodology

### 134 2.1. Geological setting

135 The Cap d'Ailly area in northern France (Fig.1) displays a series of expanded late Paleocene-early  
136 Eocene sedimentary sections corresponding to terrestrial and lagoonal environments that outcrop on  
137 top of the Cap d'Ailly cliffs (Dupuis et al., 1998; Magioncalda et al., 2001). These Paleogene  
138 sediments are divided into three Formations (Fig.2; Dupuis et al., 1998): (i) the Mortemer Fm is best  
139 known for its uppermost lacustrine-palustrine Member, the "Calcaire du Cap d'Ailly" (CCA) Mb; (ii)  
140 the Soissonnais Fm begins with the lagoonal "Sables et Argiles à Ostracodes et Mollusques" (SAOM)  
141 Mb that is overlain by the marine clay of the Craquelins Mb (Fig. 2); (iii) the transgressive  
142 Varengeville Fm first displays three glauconitic clayey sand units (FV1 to FV3) that are overlain by  
143 two clay units (FV4 and FV5) separated from each other by a glauconitic and bioclastic sand bed. In  
144 this area, previous studies have established the Paleocene-Eocene boundary (P-Eb) and the PETM  
145 within the CCA Mb, in the L1 lignite complex (Magioncalda et al., 2001). They also revealed the  
146 presence of four less pronounced negative carbon isotope peaks and excursions: P<sub>1</sub>, P<sub>2</sub>, CIE2 and CIE3  
147 (Fig. 2; Magioncalda, 2004). Finally, nanofossils of the NP11 biozone were found across the junction

148 of units FV4 and FV5 (Aubry, 1983) indicating that their age is younger than the PETM by at least 1.6  
149 Ma (Vandenberghe et al., 2012).

150 The Phare d'Ailly borehole, drilled by the BRGM near the Cap d'Ailly section, displays 9 m of  
151 Sparnacian sediments, including 1.8 m of the CCA Mb, 6.1 m of the SAOM Mb and 95 cm of the  
152 Craquelins Mb (Fig. 3). The CCA Mb is mainly characterized by 1 m of lignite and alternations of  
153 organic-rich marl, silt and clay beds that overlay fluvial sands and a lacustrine limestone. The SAOM  
154 Mb, split in two units by a lignite complex L2 and its subjacent paleosol, displays an alternation of  
155 sand, silt, clay and coquina beds. The uppermost SAOM is also characterized by the presence of oyster  
156 shells and of a siderite nodules bed that marks the base of a decalcification interval at its top. Finally,  
157 the Craquelins Clay Mb consists of dark green glauconitic clay and silts.

## 158 *2.2. Bulk organic matter $\delta^{13}C$*

159 66 samples from the Phare d'Ailly core were prepared according to the method described by  
160 Magioncalda et al. (2004) and modified by Yans et al. (2010). After decarbonation, organic matter  
161 (OM) enriched residues were analyzed with a ThermoFinnigan Flash EA 1112 coupled with a  
162 ThermoFinnigan Delta Vplus mass spectrometer (MS).  $\delta^{13}C$  values based on duplicate analyses were  
163 calculated against a calibrated CO<sub>2</sub> gas and normalized to the VPDB scale.

## 164 *2.3. Lipid extraction, separation and analysis*

165 30 dried and powdered samples were extracted with an Accelerated Solvent Extractor (ASE 200,  
166 Dionex©) using a solvent mixture of dichloromethane (DCM):methanol 9:1 (v/v). Extracted lipids  
167 were first separated by solid phase extraction into neutrals and acidic compounds and then into  
168 aliphatic hydrocarbons and polar compounds with Kieselgel-type-silica columns, according to the  
169 protocol described in Garel et al. (2013). The aliphatic hydrocarbons were dissolved in toluene and 5 $\alpha$ -  
170 Cholestane was added as internal standard.

171 GC-MS analyses were performed on a Trace GC Ultra interfaced with a TSQ Quantum XLS MS. The  
172 GC was fitted with a Trace Gold TG-5 MS capillary column (60 m x 0.25 mm i.d., 0.25  $\mu$ m film  
173 thickness). GC operating conditions were as follows: temperature hold at 40 °C for 1 min, then an



174 increase from 40 to 120 °C at 30 °C/min, 120 to 300 °C at 3 °C/min with a final isothermal hold at 300  
175 °C for 70 min. Samples were injected in splitless mode in a 2 µl volume with the injector temperature  
176 at 280 °C. Helium was the carrier gas at a constant flow rate of 1 ml/min. *n*-alkanes were then  
177 identified and quantified by measuring the areas of their peaks on the *m/z* 57 + 71 + 85 ions specific  
178 chromatograms. These areas were converted to areas on the Total Ion Current chromatogram using a  
179 correction factor and normalized to the peak of standard and weight of dry sample extracted.

#### 180 2.4. Compound-specific isotopic compositions ( $\delta^{13}\text{C}$ and $\delta^2\text{H}$ )

181 The carbon isotopic composition ( $\delta^{13}\text{C}$ ) and the hydrogen isotopic composition ( $\delta^2\text{H}$ ) of the *n*-C<sub>27</sub> and  
182 *n*-C<sub>29</sub> alkanes were determined by gas chromatography-isotope ratio mass spectrometry (GC-irMS)  
183 using a Trace GC chromatograph equipped with a TriPlus autosampler, connected to a GC-isolink  
184 combustion (for  $\delta^{13}\text{C}$ ) or pyrolysis (for  $\delta^2\text{H}$ ) interface. Operating conditions were the same as those  
185 described in Garel et al. (2013). All  $\delta^{13}\text{C}$  values were determined at least in duplicate and  $\delta^2\text{H}$  in  
186 triplicate. They were averaged to obtain a mean value, and normalized to the VPDB and VSMOW  
187 scales, respectively.

#### 188 2.5. Palynofacies

189 33 samples were manually crushed and treated with HCl and HF to remove the mineral matrix.  
190 Palynofacies observations were performed using an Axioplan2 Imaging Zeiss microscope under  
191 transmitted light and UV excitation (Zeiss HBO 100 Microscope Illuminating System, mercury short-  
192 arc lamp) with a magnification of 630. Organic facies were examined, and approximately 2000  
193 surface units per sample were counted and classified according to the methods of Tyson (1995) and  
194 Batten (1996) later modified by Garel et al. (2013).

#### 195 2.6. K-Ar measurements

196 Two units containing abundant glauconite grains, CR and FV5, were found relevant for pertinent  
197 radiometric dating. Glauconite grains are embedded in the clay matrix or concentrated in  
198 autochthonous bioturbations, suggesting that they formed *in situ*. In addition, diverse steps of  
199 glauconitization from Fe-illite to mature glauconite were recorded during the preparation of the

200 samples, which also point to an *in situ* contemporaneous origin. K-Ar dating was carried out on two  
201 samples of glauconite grains: 1) sample GL-CRA from the Craquelins Mb, and 2) sample GL-92A64  
202 from the FV5 unit.

203 About 1.5 g of grains of glauconite was isolated following the procedure recommended by Odin and  
204 Matter (1981). The sediment was first washed with triple distilled water and dried at 45°C. The  
205 sediment was then sieved at 210 µm and 420 µm. The separation of glauconite grains in the  
206 granulometric fraction between 210 and 420 µm was performed using a Frantz magnetizer (intensity  
207 of 0.5 A and tilt of 9°). The final purification was achieved under an optical microscope by hand  
208 picking the remaining impurities. Then, the grains of glauconite underwent ultrasonic cleaning (30  
209 seconds for the first step and 2 minutes for the second step) to clean the cracks developed during the  
210 growth of glauconite grains.

211 The isotopic composition and abundance of Ar were determined at the LSCE ('Laboratoire des  
212 Sciences du Climat et de l'Environnement', Gif/Yvette, France), using an unspiked technique  
213 described by Charbit et al. (1998). The mass spectrometer sensitivity is  $5.7 \times 10^{-3} \text{ mol/A } \Omega \text{ m/e} = 40$   
214 with amplifier backgrounds of  $75 \times 10^{-12} \text{ A } \Omega \text{ m/e} = 40$  ( $10^9$  ohm resistor), and  $5.75 \times 10^{-14} \text{ A } \Omega \text{ m/e} =$   
215  $36$  ( $10^{11}$  ohm resistor).

216 Replicate unspiked K-Ar age determinations were done on both samples. Argon was extracted by  
217 radio frequency heating of 0.4 – 0.7 g of sample, then transferred to an ultra-high-vacuum glass line  
218 and purified with titanium sponge and Zr-Ar getters. Isotopic analyses were performed on total  $^{40}\text{Ar}$   
219 contents ranging between  $1.0$  and  $1.5 \times 10^{-9}$  moles using a  $180^\circ$ , 6 cm radius mass spectrometer with  
220 an accelerating potential of 620V. The spectrometer was operated in static mode, but its volume was  
221 varied to give equal  $^{40}\text{Ar}$  signals for the air aliquots and the samples. Beam sizes were measured  
222 simultaneously on a double Faraday collector in sets of 100 online acquisitions with a 1 s integration  
223 time. The atmospheric correction was monitored via a separate measurement of a manometrically-  
224 calibrated dose of atmospheric argon for each sample (from a separate reservoir of known  $^{40}\text{Ar}$   
225 content). Periodic cross-calibration of zero-age standards precisely constrained the mass-  
226 discrimination to within  $\pm 0.5\%$  on the  $^{40}\text{Ar}/^{36}\text{Ar}$  ratios.

227 The manometric calibration of the Air reference is based on periodic, replicate determinations of  
228 international dating standards of known K-Ar age using the same procedure for the unknowns as  
229 described in Charbit et al. (1998). This allows the total  $^{40}\text{Ar}$  content of the sample to be determined  
230 with a precision of about  $\pm 0.2\%$  ( $2\sigma$ ). Standards used include LP-6 ( $127.8 \pm 0.7$  Ma, Odin, 1982) and  
231 HD-B1 -  $24.21 \pm 0.32$  Ma (Hautmann and Lippolt, 2000 and references herein). At the 95%  
232 confidence level, the values adopted here are consistent with those obtained for several  $^{40}\text{Ar}/^{39}\text{Ar}$   
233 standards through the intercalibration against biotite GA-1550 by Renne et al. (1998) and Spell and  
234 McDougall (2003). Uncertainties for the K and Ar data are  $1\sigma$  analytical only and consist of  
235 propagated and quadratically averaged experimental uncertainties arising from the K,  $^{40}\text{Ar}$  (total), and  
236  $^{40}\text{Ar}^*$  determinations.

237

### 238 3. Results

#### 239 3.1. $\delta^{13}\text{C}$ values of bulk OM and *n*-alkanes

240 Bulk OM is enriched in  $^{13}\text{C}$  compared to *n*-C<sub>27</sub> and *n*-C<sub>29</sub> alkanes over the record, with  $\delta^{13}\text{C}$  values  
241 ranging from  $-22.3\text{‰}$  to  $-31.8\text{‰}$ , from  $-28\text{‰}$  to  $-33.8\text{‰}$  and from  $-27.2\text{‰}$  to  $-31.9\text{‰}$ , respectively.  
242 The lowest  $\delta^{13}\text{C}$  values are found within the L1 complex (Fig.3), whereas the highest ones are found at  
243 the top of L1 for *n*-alkanes and within the SAOM base for bulk OM. Three negative excursions are  
244 observed in all curves: (i) the CIE1 located within the L1 between 40.6 and 40.2 m, with an amplitude  
245 of  $5\text{‰}$ ,  $4\text{‰}$  and  $3\text{‰}$  for bulk OM, *n*-C<sub>27</sub> and *n*-C<sub>29</sub> respectively; (ii) the CIE2 located within the upper  
246 SAOM between 35.72 and 34.7 m, with an amplitude of  $3.5\text{‰}$ ,  $2.2\text{‰}$  and  $1.4\text{‰}$  for bulk OM, *n*-C<sub>27</sub>  
247 and *n*-C<sub>29</sub> respectively; and (iii) the CIE3 within the Craquelins Mb (up to 33.3 m), which may begin  
248 in the uppermost SAOM (34.4 m), with an amplitude of  $2.5\text{‰}$ ,  $3\text{‰}$  and  $2.5\text{‰}$  for bulk OM, *n*-C<sub>27</sub> and  
249 *n*-C<sub>29</sub>. These three CIEs were first unraveled by Magioncalda, (2004) in the Cap d'Ailly section, where  
250 they are recorded in the same stratigraphic units. Two additional negative peaks (i.e. with a lower  
251 vertical extension compared to CIEs) are also observed: P<sub>1</sub> in the lower SAOM (38.75 m) with a  
252 magnitude of  $2.9\text{‰}$  that is not observed in *n*-alkanes  $\delta^{13}\text{C}$  values due to the lower resolution of GC-

253 irMS analyses in this interval; and P<sub>2</sub> in the paleosol and L2 complex at the top of the lower SAOM  
254 (36.55 m) with a magnitude of 2‰, 1.3‰ and 3‰ for bulk OM, *n*-C<sub>27</sub> and *n*-C<sub>29</sub> respectively. These  
255 two peaks were also observed by Magioncalda (2004) in the Cap d'Ailly section (Fig.2).

### 256 3.2. Palynofacies

257 Three main OM groups are observed (Fig.4): (i) gelified OM corresponding to plant tissues that  
258 suffered gelification (Batten, 1996); (ii) amorphous OM with a strong green fluorescence that has a  
259 freshwater algal origin in the Cap d'Ailly area (Garel et al., 2013); and (iii) diffuse non-fluorescent  
260 amorphous OM corresponding to degraded OM from various sources. Three kinds of plant debris are  
261 also seen: brown wood, opaque and translucent phytoclasts. Furthermore, marine dinocysts and  
262 freshwater Chlorococcale algae *Pediastrum* (family: Hydrodictyaceae) are also found in abundance.  
263 OM groups with low relative proportions, such as spore/pollen and opaque phytoclasts are not  
264 discussed here (see Supplementary Data).

265 In the Phare d'Ailly core, the lignite complexes L1 and L2 are dominated by gelified OM (i.e. > 50  
266 %), except for three samples of the L1 where degraded OM is dominant (Fig.5). SAOM and  
267 Craquelins samples are dominated by degraded OM except for one sample where gelified particles are  
268 dominant. Algal amorphous OM displays relative proportions up to 30 %, the highest proportions  
269 occurring in CIEs 1 and 2 intervals, whereas the lowest proportions are encountered in the SAOM and  
270 Craquelins Mbs. *Pediastrum* algae show very high concentrations in CIEs 1 and 2 intervals (up to 20  
271 %), whereas they only display low to very low concentrations in other samples. Finally, dinocysts that  
272 are first encountered in the L1 summit display two intervals of strong concentrations: the first at the  
273 base of the SAOM Mb, the second beginning just above the L2 and extending to the base of CIE2.

### 274 3.3. Higher plant *n*-alkanes

275 The *n*-alkane distribution in the studied samples shows a dominance of long-chain leaf-wax *n*-alkanes.  
276 Their average chain length (ACL) can be calculated using the following equation (where C<sub>x</sub> refers to  
277 the peak area of the individual alkane):

$$278 \text{ACL} = (25 \times C_{25} + 27 \times C_{27} + 29 \times C_{29} + 31 \times C_{31} + 33 \times C_{33} + 35 \times C_{35}) / (C_{25} + C_{27} + C_{29} + C_{31} + C_{33} + C_{35})$$

279 ACL values range between 28 and 29.2 (Fig.5). The highest values ( $> 29$ ) are found at the base of the  
280 core, just below the CIE1 and within the lower SAOM, whereas the lowest ones are associated with  
281 CIE1, CIE2 and the isotopic peak P<sub>2</sub>.

282 Previous studies on *n*-alkane distribution revealed a clear relationship between the climate, especially  
283 moisture in the environment, and its related type of vegetation and the ACL (e.g. Eley and Hren, 2018;  
284 Rommerskirchen et al., 2003; Schwark et al., 2002). Indeed, it appears that *n*-alkanes from vegetation  
285 growing under favorable climatic conditions (i.e. temperate or equatorial) display lower ACL values,  
286 whereas *n*-alkanes from plants subjected to harsh conditions (i.e. arid or boreal) show a higher ACL.  
287 Therefore, this proxy can be used as a complementary tool to decipher paleoclimatic conditions, and,  
288 in particular, paleohydrology.

### 289 3.4. $\delta^2H$ values of *n*-alkanes

290 Along the Phare d'Ailly core, similar trends are observed for the  $\delta^2H$  values of both C<sub>27</sub> and C<sub>29</sub> *n*-  
291 alkanes, *n*-C<sub>29</sub> being generally more depleted in <sup>2</sup>H (Fig.3).  $\delta^2H$  values range between  $-114\text{‰}$  and  
292  $-202\text{‰}$  for the *n*-C<sub>27</sub> and between  $-119\text{‰}$  and  $-202\text{‰}$  for the *n*-C<sub>29</sub>. The lowest values are observed  
293 below the CIE1 and the highest just below CIE2. The CIE1 and the interval immediately below are  
294 marked by high frequency changes in  $\delta^2H$  values of both *n*-alkanes. In the lower SAOM a less  
295 negative peak precedes a decreasing trend that ends at the lignite complex L2 where *n*-alkanes  $\delta^2H$   
296 values reach  $-185\text{‰}$ . Above the maximum peak,  $\delta^2H$  values are around  $-180\text{‰}$  until the top of the  
297 Craquelins Mb where a less negative peak is observed.

### 298 3.5. Radiometric K-Ar ages on glauconite

299 K-Ar datings are given in Table 1. The K-Ar ages of the replicates of the sample GL-CRA are  $54.4 \pm$   
300  $0.8$  Ma and  $53.6 \pm 0.8$  Ma; the K-Ar ages of the replicates of the sample GL-92A64 are  $53.1 \pm 0.8$  Ma  
301 and  $52.8 \pm 0.7$  Ma. Altogether, these data show very consistent ages of  $54.0 \pm 0.8$  Ma and  $52.95 \pm 0.8$ ,  
302 respectively. The K<sub>2</sub>O content of the GL-CRA is 5.71% and 6.63 % for GL-92A64.

## 303 4. Discussion

#### 304 4.1. Reliability of the carbon isotopic data as stratigraphic marker

305 The negative carbon isotope excursions of the early Eocene hyperthermals are recorded in both  
306 carbonates and sedimentary organic matter (Krishnan et al., 2014; Magioncalda et al., 2004).  $\delta^{13}\text{C}_{\text{org}}$   
307 value mainly depends on the source of bulk organic matter (e.g. algae, bacteria and/or land plants) and  
308 the  $\delta^{13}\text{C}$  value of atmospheric  $\text{CO}_2$ , but is also controlled by several minor factors (for more details see  
309 Meyers, 1997 and Tyson, 1995) including: the water temperature during algae biosynthesis and local  
310 environmental parameters (e.g. moisture and luminosity). As demonstrated by previous studies (Garel  
311 et al., 2013; Magioncalda et al., 2001), the Cap d'Ailly area was marked by important changes in OM  
312 sources during the late Paleocene and the early Eocene. It is thus necessary to decipher whether or not  
313 the  $\delta^{13}\text{C}_{\text{org}}$  peaks and excursions are mainly linked with changes in OM sources before using them as  
314 reliable chemostratigraphic markers. This is why the  $\delta^{13}\text{C}$  values of long-chain *n*-alkanes are precious  
315 as they are mainly derived from higher plant leaf waxes (Eglinton and Hamilton, 1967), and thus not  
316 affected by changes of OM sources.

317 First, palynofacies results have shown that the Mortemer Fm is dominated by higher plant (i.e. gelified  
318 OM) and/or freshwater algae OM (i.e. algal AOM + "*Pediastrum* spp.) whereas the Soissonnais Fm is  
319 mainly dominated by marine OM (i.e. diffuse AOM + dinocysts). Previous authors have shown that  
320 marine algae display a higher  $\delta^{13}\text{C}$  ( $\approx -26$  to  $-20\text{‰}$ ) compared to  $\text{C}_3$  plants ( $\approx -32$  to  $-23\text{‰}$ ) and  
321 freshwater algae ( $\approx -30$  to  $-25\text{‰}$ ; Meyers, 1997; Tyson, 1995). This would explain the fact that, in the  
322 Soissonnais Fm.,  $\delta^{13}\text{C}_{\text{org}}$  values are  $\approx 1.5\text{‰}$  higher than in the L1, whereas the  $\delta^{13}\text{C}_{n\text{-alkanes}}$  values are  
323 stable. Thus, it would be hazardous to compare L1  $\delta^{13}\text{C}_{\text{org}}$  values with the ones of the SAOM and  
324 Craquelins Members.

325 In Phare d'Ailly, CIE1 and CIE2 initiations are both correlated with an increase in freshwater algae  
326 concentrations (Fig. 5). Furthermore, the CIE2 initiation is also correlated with strong dinocysts  
327 concentrations. However, as both these CIEs are also seen in the  $\delta^{13}\text{C}$  curves of long-chain *n*-alkanes,  
328 it is unlikely that they are only related to a change of source of OM. Furthermore, the curve showing  
329 the highest magnitude for every CIE is systematically the  $\delta^{13}\text{C}_{\text{org}}$  one. This suggests that the increase in

330 freshwater algal OM associated with these excursions has led to a stronger drop of  $\delta^{13}\text{C}$  values in the  
331 bulk OM than in the long-chain  $n$ -alkanes.

332 Regarding CIE2, one could argue that it is only validated by one  $\delta^{13}\text{C}_{n\text{-alkanes}}$  sample and that the main  
333 part of CIE2 observed in  $\delta^{13}\text{C}_{\text{org}}$  values is linked with the change of OM sources stated above. But this  
334 seems very unlikely as, above the peak of freshwater algae concentration, the  $\delta^{13}\text{C}_{\text{org}}$  values are still  
335 lower than the pre-CIE2 ones. This implies that, the switch from a bulk OM dominated by freshwater  
336 algae to a bulk OM dominated by marine OM only had limited effect on the  $\delta^{13}\text{C}_{\text{org}}$  values. Thus, the  
337 CIE2 is very likely caused by regional/global factors and that it can be used to establish a stratigraphic  
338 framework.

339 Palynofacies results show that there is no change in OM sources correlated with CIE3. Furthermore,  
340  $\delta^{13}\text{C}_{n\text{-alkanes}}$  values also show a decrease in the Craquelins Mb. This suggests that CIE3 is also linked  
341 with regional and/or global changes. A higher resolution in the  $\delta^{13}\text{C}_{n\text{-alkanes}}$  record would however help  
342 to have a more accurate magnitude and extent of this excursion.

343 In Phare d'Ailly, the  $\text{P}_1$  negative peak is only seen in the  $\delta^{13}\text{C}_{\text{org}}$  curve and is correlated to a peak of  
344 dinocyst concentrations (>20%; Fig. 5). A previous study has shown that organic dinocysts from the  
345 late Paleocene and the PETM display  $\delta^{13}\text{C}$  values between -27 and -20‰ (Sluijs et al., 2018), a range  
346 of values comparable to the one of marine algae ( $\approx$  -26 to -20‰; Meyers, 1997; Tyson, 1995). It is  
347 thus unlikely that an increase in dinocysts concentrations would cause a negative peak in  $\delta^{13}\text{C}_{\text{org}}$  values  
348 of the lagoonal SAOM Mb. Furthermore, the  $\text{P}_1$  negative peak has a wider extension in the Cap  
349 d'Ailly section (Fig. 2). Therefore, it is likely that this peak is not an artifact but reflects regional or  
350 global changes.

351 The  $\text{P}_2$  negative peak initiation is not associated with changes in organic sources (Fig.5). Its lower  
352 magnitude in the  $\delta^{13}\text{C}_{n\text{-alkanes}}$  curve is likely due to the fact that the sample with the pre- $\text{P}_2$  highest  
353  $\delta^{13}\text{C}_{\text{org}}$  value (at -37.58 m) was not analyzed with a GC-irMS. A higher resolution in the  $\delta^{13}\text{C}_{n\text{-alkanes}}$   
354 record would thus help to accurately determine the magnitude and extent of this peak.

355 It thus seems that all these negative peaks and excursions are not related to changes in OM sources.  
356 This implies that they are linked with regional/global factors and that they can be used as stratigraphic  
357 markers, at least in the Paleocene-Eocene sites of the region.

#### 358 4.2. Litho- Bio- and Chemo-stratigraphy, and K-Ar dating

359 K-Ar dating methods on glauconite grains have been widely used to date sedimentary successions (see  
360 a synthesis in Clauer et al., 2005). The K<sub>2</sub>O contents of the samples are close to or higher than 6%,  
361 suggesting that the grains of glauconite have a sufficient degree of evolution to provide reliable K-Ar  
362 dating (Odin and Matter, 1981). All these data show ages younger than the age of the P-Eb (55.93 Ma;  
363 Westerhold et al., 2018) and also younger than the end of the PETM interval (~200 ka after P-Eb;  
364 Murphy et al., 2010). The age of the lower sample ( $54.0 \pm 0.8$  Ma) is logically older than the age of  
365 the upper sample in the succession ( $52.95 \pm 0.8$ ), suggesting an evolution in the formation of  
366 glauconite grains of the two studied samples.

367 Biostratigraphically, the lowermost Sparnacian sediments of the Cap d'Ailly area (i.e. units SP1 and  
368 SP2; Fig. 2) are within the *Peckichara disermas* charophyte biozone that is correlative to the NP9  
369 nannoplankton biozone (Aubry et al., 2005; Magioncalda et al., 2001). Furthermore, previous isotopic  
370 studies on organic matter in other Cap d'Ailly sites located the P-Eb and the CIE of the PETM in the  
371 Lignite complex L1 (Garel et al., 2013; Magioncalda et al., 2001; Storme et al., 2012). In the Phare  
372 d'Ailly core, the CIE1 is also found in the L1. This indicates that the CIE1 initiation corresponds to  
373 the P-Eb and that the upper part of the L1 complex was deposited during the PETM.

374 In the Varengeville Formation, the presence of *Axiodinium lunare* and *Sophismatia crassiramosa*  
375 dinoflagellates in the FV2 and FV3 units, respectively (Iakovleva, 2016; Fig. 2), points to the dinocyst  
376 biozone *Stenodinium meckefeldense* (*W. meckefeldensis* in Vandenberghe et al., 2012), which is  
377 correlated with the upper NP10 nannoplankton biozone (Fig.6; Vandenberghe et al., 2012). Moreover,  
378 in the upper FV4 and lower FV5 units, former studies revealed nannoplankton species corresponding  
379 to the NP11 biozone (Aubry, 1983). This is in agreement with the K-Ar age obtained on FV5



380 glauconite grains (i.e. 53.75 +/- 0.8 Ma; Fig. 6), as the NP11 biozone extends from 54.17 to 53.6 Ma  
381 (Vandenberghe et al., 2012).

382 SP3 and SP4 units (i.e. the SAOM Mb) are thus younger than the P-Eb and older than the NP11  
383 biozone (Fig. 6), which is consistent with the K-Ar age found in the Craquelins Mb (i.e. 54 Ma +/-  
384 0.8). The SAOM and Craquelins Members are characterized by an *Apectodinium* acme (Fig. 6), which  
385 would point to a PETM age in the Dieppe-Hampshire Basin (Iakovleva, 2016). However, regarding  
386 the Craquelins Mb, a deposition during the PETM is not supported by the glauconite K-Ar ages (54.0  
387 ± 0.8 Ma) that are, at minima, ≈ 0.93 Ma younger than the end of the PETM (≈ 55.73 Ma; Westerhold  
388 et al., 2018).

389 Considering these data, we can put forward two hypotheses regarding the age of the CIE2, CIE3 and  
390 SAOM and Craquelins Members:

- 391 1) As suggested by the dinoflagellate record (Iakovleva, 2016), the SAOM Member is interpreted  
392 to have been deposited during the PETM. This implies that the zigzag shape of the  $\delta^{13}\text{C}$  curves  
393 between the P-Eb and the Varengeville Formation, including CIE2, is the result of  
394 local/regional environmental changes. As stated before, the negative peaks and excursions  
395 found in the Cap d'Ailly area are not related to varying inputs of terrestrial OM in a lagoonal  
396 environment. Thus, if not associated to global causes, a return to pre-PETM  $\delta^{13}\text{C}$  values  
397 between the two CIEs could only be explained by environmental factors such as a strong  
398 decrease in regional moisture, in light exposure, or in available nutrients, and/or by major  
399 changes within the local/regional vegetation (Tappert et al., 2013).
- 400 2) As suggested by the isotopic record of both sites, the CIE2 may represent another isotopic  
401 event with an age corresponding to the nannofossil biozone NP10, which excludes ETM-2 and  
402 posterior events. As suggested by the cyclostratigraphic study of Cramer et al. (2003) on  
403 oceanic sites, the candidates are the E1, E2, F and G events. In the Cap d'Ailly area, the lack  
404 of more precise stratigraphic data excludes any refined age. However, if we consider the shape  
405 of the  $\delta^{13}\text{C}_{\text{org}}$  curve at Cap d'Ailly section and in the Phare d'Ailly core (Figs. 2 and 3), the  
406 negative carbon isotope peaks P<sub>1</sub> and P<sub>2</sub> could represent events E1 and E2, implying that CIE2

407 corresponds to the F event. CIE3 could then correspond to the G event, which is in agreement  
408 with glauconite K/Ar ages (Fig. 6). However, a better resolution of *n*-alkane  $\delta^{13}\text{C}$  curves is  
409 required to more accurately determine the vertical extension and magnitude of these  
410 excursions. Finally, this hypothesis implies that the dinocyst record in the Cap d'Ailly  
411 Soissonnais Fm (Iakovelva, 2016), including an *Apectodinium* acme, is not related to the  
412 PETM. This suggests that this specific assemblage is thus a consequence of the relative  
413 isolation of the Dieppe-Hampshire Basin during the early Eocene (Dupuis and Thiry, 1998),  
414 allowing a different evolution of the dinoflagellate population than the one observed in the  
415 North Sea. Furthermore, in our area, the *Apectodinium* acme would only be related to very  
416 favorable environmental conditions not necessarily linked with hyperthermal events. Actually,  
417 very high percentages of *Apectodinium* spp. have already been observed in other mid- and  
418 high-latitude successions, before and after the PETM (e.g. Bijl et al., 2013; Sluijs et al., 2005;  
419 2006; 2011).

420 To determine which hypothesis is correct, additional analyses are required such as temperature records  
421 to determine the duration of the PETM hyperthermal event in this key area.

#### 422 4. 3. Early Eocene paleoenvironmental changes

423 The L1 lignite complex of the Cap d'Ailly area is thought to have been deposited in a swamp  
424 environment that experienced strong environmental changes (Garel et al., 2013; Magioncalda et al.,  
425 2001). The strongest change occurred at the P-Eb with an abrupt change in OM distribution (Fig. 5).  
426 Indeed, whereas gelified OM dominates Paleocene samples, the CIE1 coincides with peaks of algal  
427 OM proportions, including *Pediastrum* algae. Thus, the P-Eb is marked by a switch from dominant  
428 allochthonous higher plant OM inputs to dominant autochthonous aquatic inputs. This suggests an  
429 evolution from a marsh pond to a more open and deeper swamp environment, similar to those  
430 recorded in Vasterival (France; Garel et al., 2013) and in Cobham (England; Collinson et al., 2007;  
431 Inglis et al., 2019). Furthermore, high concentrations in *Pediastrum* algae are generally associated  
432 with eutrophic water environments and strong seasonal nutrient, and thus clastic, inputs (Tyson, 1995).  
433 This is also supported by the disappearance of *Unio* shells in the upper half of the L1 lignite complex

434 in the whole area (Garel et al., 2013), a mollusk that cannot live in environments marked by high  
435 detrital inputs (Good, 2004). Therefore, the CIE1 in the Cap d'Ailly area appears to be marked by  
436 stronger detrital and nutrient inputs that enabled phytoplankton blooms causing eutrophication of the  
437 water column.

438 The end of CIE1 is encountered at the top of the L1 lignite complex and it coincides with the  
439 appearance of dinoflagellate cysts and a decrease in algal OM proportions (Fig. 5). This points to a  
440 significant marine influence in the swamp environment (Tyson, 1995) that would have caused a  
441 decline of freshwater algae such as *Pediastrum*, which is stenohaline and cannot sustain significant  
442 salinity variations (Tyson, 1995). This marine influence then increases upward, leading to the  
443 drowning of peat mires as seen in other localities of NW Europe (Collinson et al., 2007; Garel et al.,  
444 2013; Magioncalda et al., 2001; Methner et al., 2019), to eventually allow the setup of a lagoonal  
445 environment and the deposition of the SAOM Mb. It has been shown that an increase in salinity results  
446 in an increase in higher plant  $\delta^{13}\text{C}$  values (Ladd and Sachs, 2013). Thus, the return to less negative  
447  $\delta^{13}\text{C}$  values in the uppermost L1 is probably caused by the increasing marine influence, a hypothesis  
448 already proposed for the Vasterival section (Garel et al., 2013).

449 In the lower SAOM Mb, the degraded OM dominates all the samples, thus pointing to a relatively well  
450 oxygenated environment (Tyson, 1995) in agreement with the numerous coquinas and tidal sand  
451 laminae present in this Member. Moreover, significant dinocyst concentrations of the genus  
452 *Apectodinium* are observed between 39 and 38 m depth, close to the P<sub>1</sub> negative isotopic peak (Fig. 5).  
453 These dinoflagellate blooms in coastal areas indicate higher detrital and nutrient inputs (Crouch et al.,  
454 2003) compared to the rest of the lower SAOM Mb.

455 Above, the lignite complex L2 is characterized by the disappearance of dinocysts and the dominance  
456 of gelified OM derived from plants, in agreement with its swamp origin. The upper SAOM and  
457 Craquelins Members show a dominance of degraded OM (Fig. 5). The base of the upper SAOM Mb is  
458 marked by an increasing trend in dinocyst proportions that ends at the base of CIE2. This trend is  
459 accompanied and followed by high concentrations in freshwater algal material including *Pediastrum*,  
460 that diminishes in the second part of CIE2. It is surprising to find such quantities of freshwater

461 material in lagoonal sediments, as indicated by the fauna present in these beds (Dupuis et al., 1998).  
462 The presence of such quantities of stenohaline algae can only be explained by extensive freshwater  
463 inputs from land that probably impacted the dinoflagellate population. Furthermore, such an  
464 abundance in *Pediastrum* algae also indicates the presence of a eutrophic environment inland, a  
465 possible consequence of a climate with stronger seasonality (Tyson, 1995). It thus appears that the  
466 onset of CIE2 is linked to strong environmental changes within the lagoonal environment of the Cap  
467 d'Ailly area, with dinoflagellate blooms and extensive freshwater inputs, but also on land with  
468 eutrophication and algal blooms in the catchment area linked to the lagoon.

469 Finally, no evidence of strong environmental changes was found within the CIE3 interval. However,  
470 as the distance from the coast and depth increased at the end of the Soissonnais Fm (Dupuis et al.,  
471 1998), it is less likely to record changes that occurred on land.

#### 472 *4.4. Paleohydrological changes*

##### 473 *4.4.1 Factors controlling terrestrial n-alkane $\delta^2H$ values*

474 The hydrogen isotopic composition ( $\delta^2H$ ) of higher plant leaf wax *n*-alkanes is mainly impacted by the  
475  $\delta^2H$  of meteoric waters, which itself depends on the amount of precipitation, the temperature at the  
476 precipitation site and the source of humidity (Sachse et al., 2012). It is also affected by the degree of  
477 leaf-water transpiration and soil-water evaporation that depend on climatic parameters, and by  
478 interspecific variability, which is linked to the plant physiology and biochemistry (Smith and Freeman,  
479 2006). However, previous studies on the paleovegetation of the Cap d'Ailly area revealed no  
480 correlation between vegetation changes and *n*-alkane  $\delta^2H$  values, implying that the latter are mostly  
481 linked to paleoclimatic changes and not to changes in vegetation (Garel et al., 2014; Garel-Laurin,  
482 2013). Furthermore, Garel et al. (2013) produced  $\delta^2H$  values of onocerane I, a biomarker considered  
483 specific to a limited number of angiosperm species (Jacob et al., 2004). Thus, onocerane I  $\delta^2H$  values  
484 are very unlikely affected by vegetation changes and probably only controlled by paleohydrological  
485 parameters.  $\delta^2H_{\text{onocerane I}}$  values display a similar trend as that of  $\delta^2H_{n\text{-alkane}}$  ones, implying that these  
486 later are also representative of paleohydrological changes and almost not affected by vegetation

487 changes Regarding these data and the proximity of these two sites, we consider that Phare d'Ailly  
488  $\delta^2\text{H}_{n\text{-alkanes}}$  changes are also mostly linked with paleohydrological variations.

489 In the Phare d'Ailly core,  $\delta^2\text{H}$  values range from  $-202$  to  $-114\text{‰}$  for  $\text{C}_{27}$  *n*-alkane and from  $-202$  to  
490  $-119\text{‰}$  for  $\text{C}_{29}$  *n*-alkane (Fig. 3). In the lignite complex L1, *n*-alkanes  $\delta^2\text{H}$  values display similar  
491 magnitudes to those found in the Vasterival section (Garel et al., 2013), also located in the Cap d'Ailly  
492 area. Yet, these values are lower ( $\approx 20\text{‰}$ ) in Phare d'Ailly than in Vasterival. It is unlikely that such  
493 close locations displayed different climate and/or distance from the precipitation site. Thus, it is  
494 probable that these differences in  $\delta^2\text{H}$  values are linked to a greater water availability for plants in the  
495 surroundings of the Phare d'Ailly depositional environment compared to the Vasterival one. This  
496 hypothesis is strengthened by sedimentological evidence pointing to a more restricted environment in  
497 Vasterival during the L1 deposition, such as the presence of bacterial-induced carbonate nodules that  
498 can only form within sediments of very restricted swamp environments (Garel et al., 2013).

499 A previous study has proposed a way to calculate the  $\delta^2\text{H}$  of precipitations based on long chain *n*-  
500 alkanes  $\delta^2\text{H}$  (e.g. Sachse et al., 2012). In this study, a mean fractionation value between *n*- $\text{C}_{29}$  and  
501 mean annual precipitation (MAP)  $\delta^2\text{H}$  values for major taxonomic categories of modern plant (e.g.  $\text{C}_3$   
502 angiosperms, Pteridophytes and  $\text{C}_3$  gymnosperms). Garel et al. (2014) have shown that the Cap d'Ailly  
503 Sparnacian vegetation was mostly dominated by angiosperms. So, we can apply the mean  
504 fractionation value between *n*- $\text{C}_{29}$  of  $\text{C}_3$  angiosperms and MAP ( $\epsilon_{\text{C}_{29}/\text{MAP}}$ ), which is  $-110\text{‰}$  (Sachse et  
505 al., 2012).  $\delta^2\text{H}$  precipitation values for the Phare d'Ailly site are given in the supplementary data. They  
506 range from  $-91$  to  $-9\text{‰}$  with a mean of  $-58\text{‰}$  and a median of  $69.4\text{‰}$ . These values are intermediate  
507 between the Eocene ones of Possagno (Italy;  $0$  to  $-34\text{‰}$ ) and Lillebaelt (Denmark;  $-53$  to  $-93\text{‰}$ ),  
508 which were calculated by Speelman et al. (2010). This is consistent with the intermediate latitudinal  
509 position of Cap d'Ailly compared to these two sites.

#### 510 *4.4.2 Lignite complex L1*

511 In the Phare d'Ailly core, *n*-alkane  $\delta^2\text{H}$  curves display a zigzag shape in Upper Paleocene sediments,  
512 with variations in magnitudes reaching  $25\text{‰}$  (Fig. 3). If strictly interpreted as paleoclimatic changes,

513 these values would indicate perturbations in the hydrological cycle with an alternation of dry and wet  
514 conditions (Smith and Freeman, 2006). Such variations were also found in the Vasterival section  
515 (Garel et al., 2013), thus strengthening a regional climatic cause for these environmental changes.  
516 Evidence of climatic changes at the end of the Paleocene has already been reported in several  
517 locations, such as in the London Basin (England) where evidence of increased seasonality has been  
518 observed (Collinson et al., 2007). These Upper Paleocene climatic changes were probably related to an  
519 intense episode of volcanic activity in the North Atlantic Igneous Province, maybe linked to the  
520 beginning of stage 2 described in Abdelmalak et al. (2016). This stronger volcanic activity would have  
521 led to an increase in atmospheric CO<sub>2</sub> concentrations, and thus to a progressive climate change.

522 In our site, the P-Eb is marked by a 30‰ <sup>2</sup>H depletion of *n*-alkanes, suggesting moister conditions  
523 (Smith and Freeman, 2006). The magnitudes of *n*-alkane δ<sup>2</sup>H variations at the P-Eb are stronger in  
524 Vasterival (≈ 60‰) compared to Phare d'Ailly (≈ 30‰). This difference is likely due to a greater  
525 water availability in Phare d'Ailly compared to Vasterival, as stated above. The <sup>2</sup>H depletion of *n*-  
526 alkanes at the P-Eb is followed by a <sup>2</sup>H enrichment that leads to *n*-alkane δ<sup>2</sup>H values comparable to the  
527 pre-PETM ones (Fig. 3), and points to slightly drier conditions than before. However, this change is  
528 associated with a decrease in ACL values and an increase in algal OM concentrations, both pointing to  
529 overall moister conditions (Eley and Hren, 2018; Rommerskirchen et al., 2003; Tyson, 1995).

530 Furthermore, these algal blooms suggest that the climate was marked by a stronger seasonality (Tyson,  
531 1995), which would explain the apparent discrepancy between *n*-alkanes δ<sup>2</sup>H values and palynofacies  
532 data. This agrees with the conclusions of Garel et al. (2013) that pointed to the setup of a moister  
533 climate with stronger seasonality in the Cap d'Ailly area at the early PETM. Similar changes seemed  
534 to occur in northern Spain (Pujalte et al., 2016), in the North Sea (Eldrett et al., 2014; Kender et al.,  
535 2012) and in England (Collinson et al., 2007; Inglis et al., 2019).

#### 536 4.4.3 SAOM and Craquelins Members

537 The low resolution of samples within the Craquelins Mb (Figs. 3 and 5) does not make it possible to  
538 unravel any paleoenvironmental change associated to the potential CIE3. Thus, this Member will not  
539 be discussed in this part.

540 Regarding the SAOM Mb, it is very likely that the *n*-alkanes analyzed in these sediments are  
541 representative of a wider drainage area compared to the ones found in the L1 complex, as this member  
542 corresponds to a lagoonal environment that was much more open compared to the swamp that  
543 deposited the L1 complex. Thus, *n*-alkane relative proportions and their  $\delta^2\text{H}$  values reflect  
544 paleohydrological conditions (e.g. precipitation amount, moisture and the extent of leaf- and soil-water  
545 evaporation) of a much wider area for the SAOM than for the L1. Therefore, it would be hazardous to  
546 compare SAOM data with those of the L1 complex.

547 The lower SAOM unit first shows a  $\delta^2\text{H}$  peak at  $-125\text{‰}$  for both *n*-alkanes followed by a decrease that  
548 stops in the L2 complex (Fig. 3), suggesting a progressive change to moister conditions (Smith and  
549 Freeman, 2006). The dramatic increase in dinocyst proportions that is observed at the beginning of this  
550 trend suggests that the moister conditions on land caused an increase in nutrient inputs into the lagoon,  
551 and thus, dinoflagellate blooms (Tyson, 1995).

552 Above, the first sample in the upper SAOM unit displays *n*-alkane  $\delta^2\text{H}$  values similar to the last value  
553 observed in the lower SAOM Mb (Fig. 3), suggesting a relative stability of hydrological conditions on  
554 land (Smith and Freeman, 2006). It is followed by a peak at  $-125\text{‰}$  for both *n*-alkanes just below  
555 CIE2 that points to drier conditions, followed itself by a return to more negative values in the body of  
556 CIE2, and thus moister conditions (Smith and Freeman, 2006). This last sample is also marked by  
557 lower ACL values than previously that also point to moister conditions (Eley and Hren, 2018). A  
558 similar  $\delta^2\text{H}$  pattern has been observed in the Arctic around the ETM2 event (Krishnan et al., 2014).  
559 For our sites, if we consider the hypothesis 2, the increase in  $\delta^2\text{H}$  values followed by their increase  
560 might be related to a two steps event. This is strengthened by the palynofacies data that display a  
561 strong increase in dinocyst concentrations followed by a peak in freshwater algae proportions. As for  
562 the PETM, a climatic change in two steps may be linked to a volcanic event triggering a first climatic  
563 change but also a series of events such as the release of thermogenic methane (Frieling et al., 2016)  
564 eventually causing a hyperthermal event.

565 In the Phare d'Ailly core, these hydrological changes are correlated with high concentrations of  
566 dinocysts and freshwater algae, with *Pediastrum* species appearing only after the peak of drier

567 conditions (Figs. 3 and 5). They point to the eutrophication of water masses and higher seasonality on  
568 land (Tyson, 1995) for an interval ranging from below the CIE2 base to its body. Thus, it appears that  
569 the CIE2 coincides with strong climatic changes causing dramatic environmental variations in both  
570 terrestrial and lagoonal environments. Such evidence of eutrophication has also been observed in  
571 similar sediments of the Kallo borehole (Belgium, Steurbaut et al., 2003), where a second CIE, a few  
572 meters above the end of the first CIE, is also correlated with high proportions of *Pediastrum* algae.  
573 This may indicate that CIE2 is linked to a regional event implying environmental eutrophication and a  
574 climate with stronger seasonality on land.

575 Moreover, it has to be noted that this event follows an interval of relative climatic stability (i.e. the  
576 lower SAOM unit). To our knowledge, the occurrence of two intervals of dramatic climatic and  
577 environmental changes has never been observed for the PETM alone. Moreover, except for CIE2 and  
578 L2 samples, the  $\delta^2\text{H}$  record does not seem correlated to the  $\delta^{13}\text{C}$  record, implying that the zigzag shape  
579 of the  $\delta^{13}\text{C}$  curve is not related to climate variations. Thus, this climatic succession may suggest that  
580 CIE1 and CIE2 correspond to two different events: the PETM for CIE1, and the E1, E2, F or G event  
581 for CIE2. However, to prove such a hypothesis, temperature proxies are needed to determine whether  
582 the whole Soissonnais Fm. is associated with the PETM hyperthermal event or not. In any case, this  
583 study shows for the first time either two important different environmental events within the PETM or  
584 strong environmental consequences linked with the carbon isotope events E1, E2, F or G.

## 585 Conclusions

586 New high-resolution organic matter and higher plant *n*-alkanes  $\delta^{13}\text{C}$  records along with K-Ar ages on  
587 glauconite and available stratigraphic data from two sites of the Cap d'Ailly area provide a framework  
588 to unravel climatic and environmental changes associated with Lower Eocene hyperthermals and  
589 isotopic events. Our results show five negative CIEs, the main ones being CIE1 and CIE2, within  
590 terrestrial and coastal sediments of the Sparnacian Mortemer and Soissonnais Formations, which are  
591 older than the NP11 nanofossil biozone. While the CIE1 is clearly associated with the PETM, the CIE2  
592 could either correspond to 1) a second excursion within the PETM interval, as suggested by the dinocyst  
593 record, implying that less negative  $\delta^{13}\text{C}$  values between the two CIEs are related to regional



594 environmental changes or 2) to another global isotopic event, as suggested by  $\delta^{13}\text{C}$  values and K-Ar  
595 ages, which occurred before the ETM2 such as events E1, E2, F and G. The latter hypothesis implies  
596 that the dinocyst record of the Cap d'Ailly area was affected by a different evolution compared to the  
597 North Sea, maybe due to relative isolation during this interval. In that case, other negative peaks and  
598 excursions recorded in the Cap d'Ailly likely correspond to these events.

599 Palynofacies observations indicated that both CIEs were associated with dramatic environmental  
600 changes, such as eutrophication and algal and/or dinoflagellate blooms. These changes were probably,  
601 at least, regional as they were also recorded in the Belgian Basin. Furthermore, higher plant *n*-alkanes  
602 relative proportions and  $\delta^2\text{H}$  records revealed that these intervals are linked to paleohydrological  
603 changes and higher seasonality. These data also revealed that the interval just below the CIEs is marked  
604 by environmental and paleoclimatic changes, which were already reported in other locations before the  
605 PETM and the ETM-2. Thus, our study shows for the first time either 1) a PETM marked by two distinct  
606 intervals of dramatic environmental and climatic changes; or 2) that a “minor” isotopic event, E1, E2, F  
607 or G, was associated with strong environmental and climatic changes similar to those that occurred  
608 around the P-Eb.

## 609 Acknowledgements

610 S.G. thanks the French ‘Ministère de l’Enseignement Supérieur et de la Recherche’ for a Doctoral grant.  
611 We wish to thank Florence Savignac (Sorbonne Université) for her technical support, Jean-Yves Storme  
612 for scientific discussion, Hervé Guillou for K-Ar analyses and Elizabeth Rowley-Jolivet for English  
613 revision. We also thank Vittoria Lauretano and an anonymous reviewer for their comments and reviews,  
614 which considerably improved the manuscript. This paper is a contribution to the Research cooperation  
615 contract financially supported by the BRGM (‘Paléosurface éocène–PETM’ research project) and to the  
616 BRGM Scientific Programs ‘Genèse et caractéristiques des Régolithes’ and ‘Référentiel Géologique de  
617 la France’. The work was part of the PalHydroMil project, supported by Agence Nationale de la  
618 Recherche Grant ANR-2010-JCJC-607-01. J.Y. thanks the Belgian Science Policy Office, project 688  
619 BR/121/A3/PALEURAFRICA.

620 References

- 621 Abdelmalak MM, Meyer R, Planke S, *et al.* 2016. Pre-breakup magmatism on the Vøring Margin:  
622 Insight from new sub-basalt imaging and results from Ocean Drilling Program Hole 642E.  
623 *Tectonophysics* 675: 258–274.
- 624 Abels HA, Lauretano V, van Yperen AE, *et al.* 2016. Environmental impact and magnitude of  
625 paleosol carbonate carbon isotope excursions marking five early Eocene hyperthermals in the Bighorn  
626 Basin, Wyoming. *Clim. Past.* 12: 1151–1163.
- 627 Aubry M-P. 1983. Biostratigraphie du Paléogène épicontinental de l'Europe du Nord-Ouest. Etude  
628 fondée sur les nannofossiles calcaires. *Docum. Labo Géol.* Lyon, 89 : 317p.
- 629 Aubry M-P, Thiry M, Dupuis C, Berggren WA. 2005. The Sparnacian deposits of the Paris Basin: A  
630 lithostratigraphic classification. *Stratigraphy* 2: 65–100.
- 631 Batten, DJ. 1996. Chapter 26A. Palynofacies and paleoenvironmental interpretation. In: Jansonius, J.  
632 & McGregor DC, (Eds.), *Palynology: Principles and Applications*. American Association of  
633 Stratigraphic Palynologists Foundation. pp. 1011–1064.
- 634 Charbit S, Guillou H, Turpin L. 1998. Cross calibration of K–Ar standard minerals using an unspiked  
635 Ar measurement technique. *Chem. Geol.* 50: 147–159.
- 636 Clauer N, Huggett JM, Hillier S. 2005. How reliable is the K–Ar glauconite chronometer? A case  
637 study of Eocene sediments from the Isle of Wight. *Clay Miner.* 40, 167–176.
- 638 Coccioni R, Bancalà G, Catanzariti R, *et al.* 2012. An integrated stratigraphic record of the  
639 Palaeocene–lower Eocene at Gubbio (Italy): new insights into the early Palaeogene hyperthermals and  
640 carbon isotope excursions. *Terra Nova* 24: 380–386.
- 641 Collinson ME, Steart DC, Scott AC, Glasspool IJ, Hooker JJ. 2007. Episodic fire, runoff and  
642 deposition at the Palaeocene–Eocene boundary. *J. Geol. Soc. London* 164: 87–97.

643 Cramer BS, Wright JD, Kent DV, Aubry, M-P. 2003. Orbital climate forcing of  $\delta^{13}\text{C}$  excursions in  
644 the late Paleocene–early Eocene (chrons C24n–C25n). *Paleoceanography* 18: 1097.

645 Crouch EM, Dickens GR, Brinkhuis H, *et al.* 2003. The Apectodinium acme and terrestrial discharge  
646 during the Paleocene-Eocene thermal maximum: new palynological, geochemical and calcareous  
647 nannoplankton observations at Tawanui, New Zealand. *Palaeogeogr. Palaeoclimatol. Palaeoecol.*  
648 194: 387–403.

649 Dupuis C, Steurbaut E, De Coninck J, Riveline J. 1998. The Western Argiles à Lignites facie. In:  
650 Thiry et Dupuis, (Ed.) The Paleocene/Eocene boundary in Paris basin: the Sparnacian deposits. Field  
651 trip guide. Ecole Nationale Supérieure Des Mines de Paris, *Mémoire Des Sciences de La Terre* 34: 60–  
652 71.

653 Dupuis C, Thiry M. 1998. Geological frame of the “Sparnacian.”. In: Thiry et Dupuis, (Ed.) The  
654 Paleocene/Eocene boundary in Paris basin: the Sparnacian deposits. Field trip guide. Ecole Nationale  
655 Supérieure Des Mines de Paris, *Mémoire Des Sciences de La Terre* 34: 3–12.

656 Eglinton G, Hamilton RJ. 1967. Leaf Epicuticular Waxes. *Science* 156: 1322–1335.

657 Eldrett JS, Greenwood DR, Polling M, Brinkhuis H, Sluijs A, 2014. A seasonality trigger for carbon  
658 injection at the Paleocene–Eocene Thermal Maximum. *Clim. Past.* 10: 759–769.

659 Eley YL, Hren MT. 2018. Reconstructing vapor pressure deficit from leaf wax lipid molecular  
660 distributions. *Sci. Rep. UK* 8: 3967.

661 Frieling J, Svensen HH, Planke S, Cramwinckel MJ, Selnes H, Sluijs A. 2016. Thermogenic methane  
662 release as a cause for the long duration of the PETM. *P. Natl. Acad. Sci. USA* 113: 12059–12064.

663 Garel S, Quesnel F, Jacob J, *et al.* 2014. High frequency floral changes at the Paleocene–Eocene  
664 boundary revealed by comparative biomarker and palynological studies. *Org. Geoch.* 77: 43–58.

665 Garel S, Schnyder J, Jacob J, *et al.* 2013. Paleohydrological and paleoenvironmental changes recorded  
666 in terrestrial sediments of the Paleocene–Eocene boundary (Normandy, France). *Palaeogeogr.*  
667 *Palaeoclimatol. Palaeoecol.* 376: 184–199.

668 Garel-Laurin S, 2013. Changements paléoenvironnementaux et paléoclimatiques enregistrés dans les  
669 faciès continentaux et lagunaires de la limite Paléocène-Eocène des bassins de Paris et de Dieppe-  
670 Hampshire. Apports de l'étude de la matière organique. PhD thesis, Université Pierre et Marie Curie,  
671 448 p.

672 Good SC. 2004. Paleoenvironmental and paleoclimatic significance of freshwater bivalves in the  
673 Upper Jurassic Morrison Formation, Western Interior, USA. *Sediment. Geol.* 167: 163–176.

674 Hautmann S, Lippolt HJ. 2000.  $^{40}\text{Ar}/^{39}\text{Ar}$  dating of central European K–Mn oxides — a  
675 chronological framework of supergene alteration processes during the Neogene. *Chem. Geol.* 170: 37–  
676 80.

677 Iakovleva AI. 2016. Did the PETM trigger the first important radiation of wetzelielloideans? Evidence  
678 from France and northern Kazakhstan. *Palynology* 41: 311–338.

679 Inglis GN, Farnsworth A, Collinson ME, *et al.* 2019 Terrestrial environmental change across the onset  
680 of the PETM and the associated impact on biomarker proxies: A cautionary tale. *Glo. Pla. Cha.* 181:  
681 102991

682 Jacob J, Disnar J-R, Boussafir M, *et al.* 2004. Onocerane attests to dry climatic events during the  
683 Quaternary in the tropics. *Org. Geoch.* 35: 289–297.

684 Kender S, Stephenson MH, Riding JB, *et al.* 2012. Marine end terrestrial environmental changes in NW  
685 Europe preceding carbon release at the Paleocene–Eocene transition. *Earth Planet. Sc. Lett.* 353-354:  
686 108–120.

687 Kennett JP, Stott LD. 1991. Abrupt deep-sea warming, palaeoceanographic changes and benthic  
688 extinctions at the end of the Paleocene. *Nature* 353: 225–229.

689 Krishnan S, Pagani M, Huber M, Sluijs A. 2014. High latitude hydrological changes during the  
690 Eocene Thermal Maximum 2. *Earth Planet. Sc. Lett.* 404: 167–177.

691 Ladd SN, Sachs JP. 2013. Positive correlation between salinity and n-alkane  $\delta^{13}\text{C}$  values in the  
692 mangrove *Avicennia marina*. *Org. Geoch.* 64: 1–8.

693 Lauretano V, Littler K, Polling M, Zachos JC, Lourens LJ. 2015. Frequency, magnitude and character  
694 of hyperthermal events at the onset of the Early Eocene Climatic Optimum. *Clim. Past.* 11: 1313–  
695 1324.

696 Littler K, Röhl U, Westerhold T, Zachos JC, 2014. A high-resolution benthic stable-isotope record for  
697 the South Atlantic: Implications for orbital-scale changes in Late Paleocene–Early Eocene climate and  
698 carbon cycling. *Earth Planet. Sc. Lett.* 401: 18–30.

699 Lourens LJ, Sluijs A, Kroon D, *et al.* 2005. Astronomical pacing of late Palaeocene to early Eocene  
700 global warming events. *Nature* 435 : 1083–1087.

701 Magioncalda R. 2004. Chémostratigraphie de la limite Paléocène/Eocène (CIE) fondée sur l'étude de  
702 la composition isotopique du carbone organique ( $\delta^{13}\text{C}_{\text{org}}$  ‰ PDB). Application pour la mise en  
703 corrélation de successions continentales, lagunaires et marines. PhD thesis, Faculté Polytechnique de  
704 Mons, Mons. 220p.

705 Magioncalda R, Dupuis C, Blamart D, *et al.* 2001. L'excursion isotopique du carbone organique ( $\delta^{13}\text{C}_{\text{org}}$   
706 dans les paleoenvironnements continentaux de l'intervalle Paleocene/Eocene de Varangeville  
707 (Haute-Normandie). *B. Soc. Géol. Fr.* 172: 349–358.

708 Magioncalda R, Dupuis C, Smith T, Steurbaut E, Gingerich, PD. 2004. Paleocene-Eocene carbon  
709 isotope excursion in organic carbon and pedogenic carbonate: Direct comparison in a continental  
710 stratigraphic section. *Geology* 32: 553–556.

711 McInerney FA, Wing SL. 2011. The Paleocene-Eocene Thermal Maximum: A Perturbation of Carbon  
712 Cycle, Climate, and Biosphere with Implications for the Future. *Annu. Rev. Earth Pl. Sc.* 39: 489–516.

713 Methner K, Lenz O, Riegel W, Wilde V, Mulch A, 2019. Paleoenvironmental response of  
714 midlatitudinal wetlands to Paleocene–early Eocene climate change (Schöningen lignite deposits,  
715 Germany). *Clim. Past.* 15: 1741–1755.

716 Meyers PA. 1997. Organic geochemical proxies of paleoceanographic, paleolimnologic, and  
717 paleoclimatic processes. *Org. Geoch.* 27: 213–250.

718 Murphy BH, Farley KA, Zachos JC. 2010. An extraterrestrial  $^3\text{He}$ -based timescale for the Paleocene-  
719 Eocene thermal maximum (PETM) from Walvis Ridge, IODP Site 1266. *Geochim. Cosmochim. Ac.*  
720 74: 5098–5108.

721 Noiret C, Steurbaut E, Tabuce R, *et al.* 2016. New bio-chemostratigraphic dating of a unique early  
722 Eocene sequence from southern Europe results in precise mammalian biochronological tie-points.  
723 *Newsl. Stratigr.* 49: 469-480.

724 Odin GS. 1982. Interlaboratory standards for dating purposes, in Numerical Dating in Stratigraphy. In:  
725 Odin GS, (Ed.), Numerical Dating in Stratigraphy. New York, pp. 123–158.

726 Odin GS, Matter A. 1981. De glauconiarum origine. *Sedimentology* 28: 611–641.

727 Pujalte V, Robador A, Payros A, Samsó J M. 2016. A siliciclastic braid delta within a lower Paleogene  
728 carbonate platform (Ordessa-Monte Perdido National Park, southern Pyrenees, Spain): Record of the  
729 Paleocene–Eocene Thermal Maximum perturbation. *Palaeogeogr. Palaeoclimatol. Palaeoecol.* 459:  
730 453–470.

731 Renne PR, Swisher CC, Deino AL, Karner DB, Owens TL, DePaolo DJ. 1998. Intercalibration of  
732 standards, absolute ages and uncertainties in  $^{40}\text{Ar}/^{39}\text{Ar}$  dating. *Chem. Geol.* 145: 117–152.

733 Rommerskirchen F, Eglinton G, Dupont L, *et al.* 2003. A north to south transect of Holocene  
734 southeast Atlantic continental margin sediments: Relationship between aerosol transport and  
735 compound-specific  $\delta^{13}\text{C}$  land plant biomarker and pollen records. *Geoch. Geoph. Geos.* 4(12): 1101.

736 Sachse D, Billault I, Bowen GJ, *et al.* 2012. Molecular Paleohydrology: Interpreting the Hydrogen-  
737 Isotopic Composition of Lipid Biomarkers from Photosynthesizing Organisms. *Annu. Rev. Earth Pl.*  
738 *Sc.* 40: 221–249.

739 Schwark L, Zink K, Lechterbeck J, 2002. Reconstruction of postglacial to early Holocene vegetation  
740 history in terrestrial Central Europe via cuticular lipid biomarkers and pollen records from lake  
741 sediments. *Geology* 30(5): 463-466.

742 Sluijs A, Pross J, Brinkhuis H, 2005. From greenhouse to icehouse; organic-walled dinoflagellate  
743 cysts as paleoenvironmental indicators in the Paleogene. *Earth-Sci. Rev.* 68: 281-315.

744 Sluijs A, Schouten S, Pagani M, *et al.*, 2006. Subtropical Arctic Ocean temperatures during the  
745 Palaeocene/Eocene thermal maximum. *Nature* 441: 610-613.

746 Sluijs A, Bjiil PK, Schouten S, Röhl U, Reichart G-J, Brinkhuis H, 2011. Southern Ocean warming, sea  
747 level and hydrological change during the Paleocene-Eocene thermal maximum. *Clim. Past.* 7: 47–61.

748 Sluijs A, van Roij L, Frieling J, Laks J, Reichart G-J, 2018. Single-species dinoflagellate cyst carbon  
749 isotope ecology across the Paleocene-Eocene Thermal Maximum. *Geology* 46(1): 79-82.

750 Smith FA, Freeman KH. 2006. Influence of physiology and climate on  $\delta D$  of leaf wax *n*-alkanes from  
751  $C_3$  and  $C_4$  grasses. *Geochim. Cosmochim. Ac.* 70: 1172–1187.

752 Smith T, Rose KD, Gingerich PD. 2006. Rapid Asia–Europe–North America geographic dispersal of  
753 earliest Eocene primate *Teilhardina* during the Paleocene–Eocene thermal maximum. *P. Natl. Acad.*  
754 *Sci. USA* 103: 11223.

755 Speelman EN, Sewall JO, Noone D, *et al.* 2010. Modeling the influence of a reduced equator-to-pole  
756 sea surface temperature gradient on the distribution of water isotopes in the Early/Middle Eocene.  
757 *Earth Planet. Sc. Lett.* 298: 57–65.

758 Spell TL, McDougall I. 2003. Characterization and calibration of  $^{40}Ar/^{39}Ar$  dating standards. *Chem.*  
759 *Geol.* 198: 189–211.

760 Steiger RH, Jäger E. 1977. Subcommittee on geochronology: Convention on the use of decay  
761 constants in geo- and cosmochronology. *Earth Planet. Sc. Lett.* 36: 359–362.

762 Steurbaut E, Magioncalda R, Dupuis C, van Simaey S, Roche E, Roche M. 2003. Palynology,  
763 paleoenvironments, and organic carbon isotope evolution in lagoonal Paleocene-Eocene boundary  
764 settings in North Belgium. *Geol. S. Am. S. Pap.* 369: 291–317.

765 Tappert R, McKellar RC, Wolfe AP, Tappert MC, Ortega-Blanco J, Muehlenbachs K. 2013. Stable  
766 carbon isotopes of C3 plant resins and ambers record changes in atmospheric oxygen since the  
767 Triassic. *Geochim. Cosmochim. Ac.* 121: 240–262.

768 Tyson RV. 1995. Sedimentary Organic Matter. Organic Facies and Palynofacies, Chapman and Hall,  
769 London, 650p.

770 Vandenberghe N, Hilgen FJ, Speijer RP. 2012. The Paleogene period. In: Gradstein *et al.* (Eds.), The  
771 Geological Time Scale 2012. Elsevier Science Ltd, Amsterdam, pp. 855–921.

772 Westerhold T, Röhl U, Frederichs T, *et al.* 2017. Astronomical calibration of the Ypresian timescale:  
773 implications for seafloor spreading rates and the chaotic behavior of the solar system? *Clim. Past.* 13:  
774 1129–1152.

775 Westerhold T, Röhl U, Wilkens RH, *et al.* 2018. Synchronizing early Eocene deep-sea and continental  
776 records – cyclostratigraphic age models for the Bighorn Basin Coring Project drill cores. *Clim.*  
777 *Past.* 14: 303–319.

778 Yans J, Gerards T, Gerienne P, *et al.* 2010. Carbon-isotope analysis of fossil wood and dispersed  
779 organic matter from the terrestrial Wealden facies of Hautrage (Mons Basin, Belgium). *Palaeogeogr.*  
780 *Palaeoclimatol. Palaeoecol.* 291: 85–105.

781 Yans J, Marandat B, Masure E, *et al.* 2014. Refined bio- (benthic foraminifera, dinoflagellate cysts)  
782 and chemostratigraphy ( $\delta^{13}\text{C}_{\text{org}}$ ) of the earliest Eocene at Albas-Le Clot (Corbières, France):  
783 implications for mammalian biochronology in Western Europe. *Newsletters on Stratigraphy* 47/3:  
784 331-353.

785 Zachos JC, Röhl U, Schellenberg SA, *et al.* 2005. Rapid Acidification of the Ocean during the  
786 Paleocene-Eocene Thermal Maximum. *Science*, New Series 308: 1611–1615.

787

788 **Figure captions**



789 **Figure 1:** location of the Cap d'Ailly composite section and the Phare d'Ailly borehole within the Cap  
790 d'Ailly area

791 **Figure 2:** lithology of the Cap d'Ailly composite section, compared to published  $\delta^{13}\text{C}_{\text{org}}$   
792 (Magioncalda, 2004), dinoflagellate (Iakovleva, 2016), nannoplankton (Aubry, 1983) and charophyte  
793 (Aubry et al., 2005) data along with K-Ar absolute ages on authigenic glauconite (this work). CIE  
794 (carbon isotope excursions) 1 to 3 and P<sub>1</sub> and P<sub>2</sub> correspond to negative  $\delta^{13}\text{C}$  excursions and peaks  
795 unraveled by Magioncalda, (2004). Green rectangle: interval spanned by the Phare d'Ailly core  
796 studied here. L1 and L2: lignite complex 1 and 2

797 **Figure 3:** Phare d'Ailly core lithology compared to the  $\delta^{13}\text{C}$  of bulk OM and *n*-alkane C<sub>27</sub> and C<sub>29</sub>  
798  $\delta^{13}\text{C}$  and  $\delta^2\text{H}$  isotopic composition. Shaded areas: extension of CIE 1 and 2 and a possible CIE3. See  
799 Figure 2 for Peaks P<sub>1</sub> and P<sub>2</sub>. Pal. = Paleocene

800 **Figure 4:** Palynofacies main categories: (A and B) algal amorphous organic matter under transmitted  
801 light and UV respectively; (C) gelified organic matter; (D) diffuse amorphous organic matter; (E) a  
802 *Pediastrum* algae under UV; (F) a dinoflagellate cyst under UV; (G and F) dinocysts, *Pediastrum*  
803 algae and a gelified phytoclast (GP) under transmitted light and UV respectively

804 **Figure 5:** Phare d'Ailly core palynofacies results and *n*-alkanes ACL (average chain length) values in  
805 comparison with  $\delta^{13}\text{C}$  curves

806 **Figure 6:** Tentative correlations between the Cap d'Ailly stratigraphic units (not at scale) and the  
807 International chronostratigraphic chart (Vandenberghé et al., 2012), and  $\delta^{13}\text{C}$  isotopic excursions ages  
808 (Cramer et al., 2003; Westerhold et al., 2017). It shows that negative isotopic excursions (CIE1 and  
809 CIE2) and peaks (P<sub>1</sub> and P<sub>2</sub>) are older than the *S. meckelfeldense* dinoflagellate biozone and thus than  
810 ETM2. This is based on nannoplankton (grey box, Aubry, 1983) and dinoflagellate (orange box,  
811 Iakovleva, 2016) records, K-Ar glauconite ages and the  $\delta^{13}\text{C}$  record (this work). Purple crosses  
812 between units indicate an unconformable boundary. The *S. meckelfeldensis* dinoflagellate biozone  
813 interval (orange box) is deduced from the first occurrence of *A. lunare* (Iakovleva, 2016).

814 Dinoflagellate first and last occurrences are from Vandenberghe et al. (2012) latter modified by  
815 Iakovleva (2016). Pal. = Paleocene. Tha. = Thanetian

816 **Table 1:** K-Ar ages of glauconites. Age calculations are based on the decay and abundance constants  
817 from Steiger and Jäger (1977). Analyzed grains were *in-situ* unweathered glauconite without  
818 contamination of micas

819

820

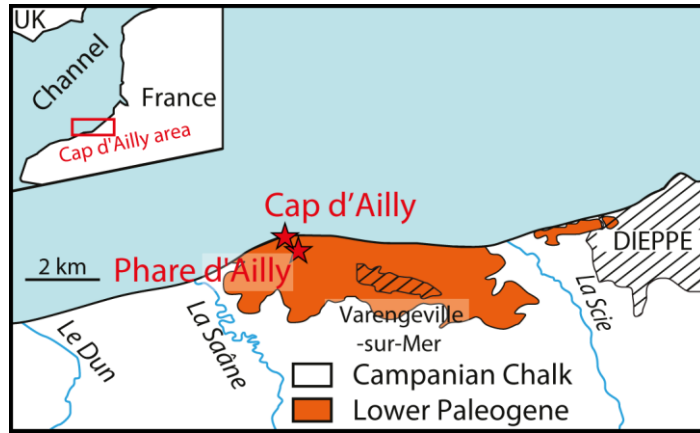
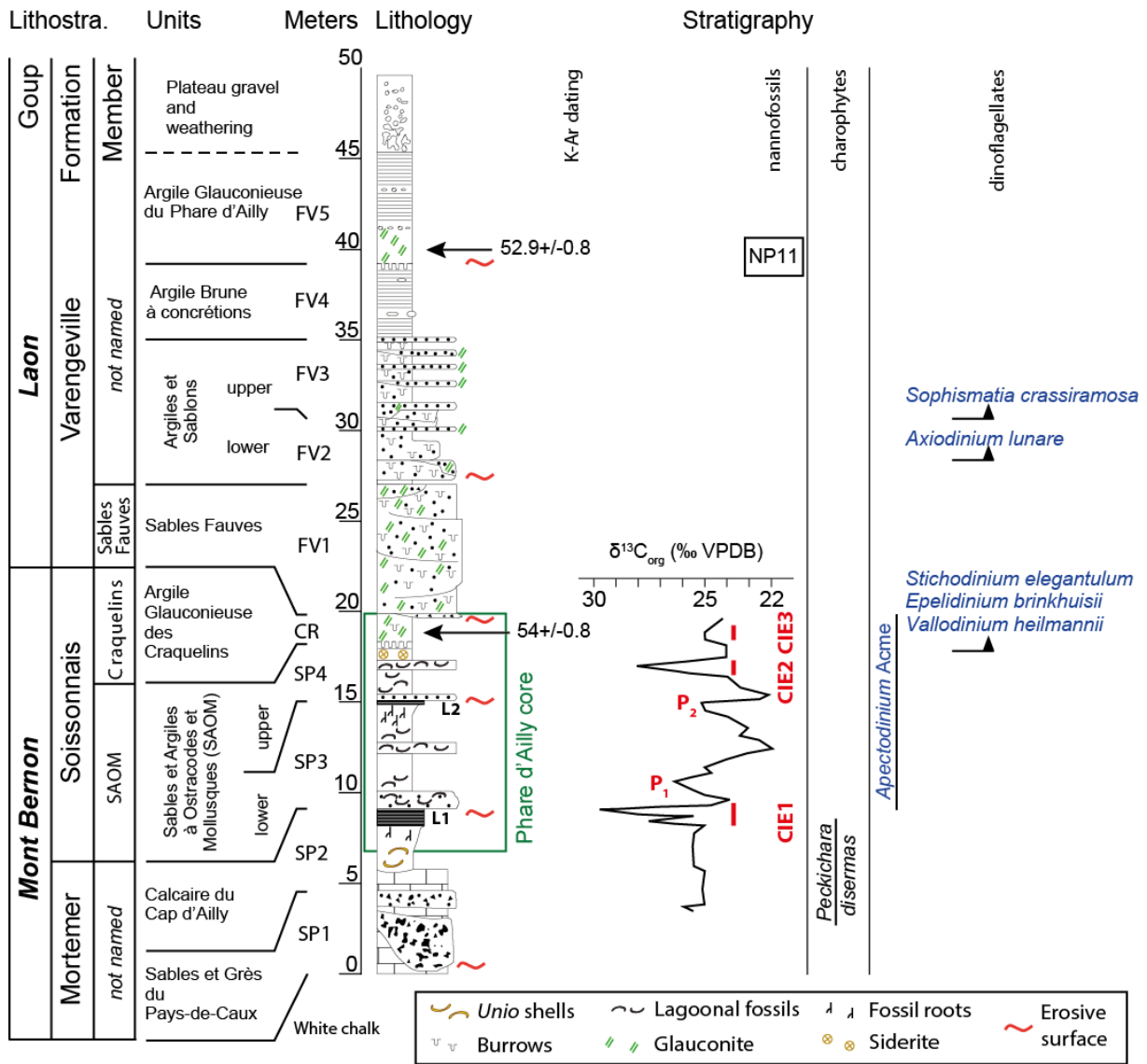


Figure 1



821

822

Figure 2

823

824

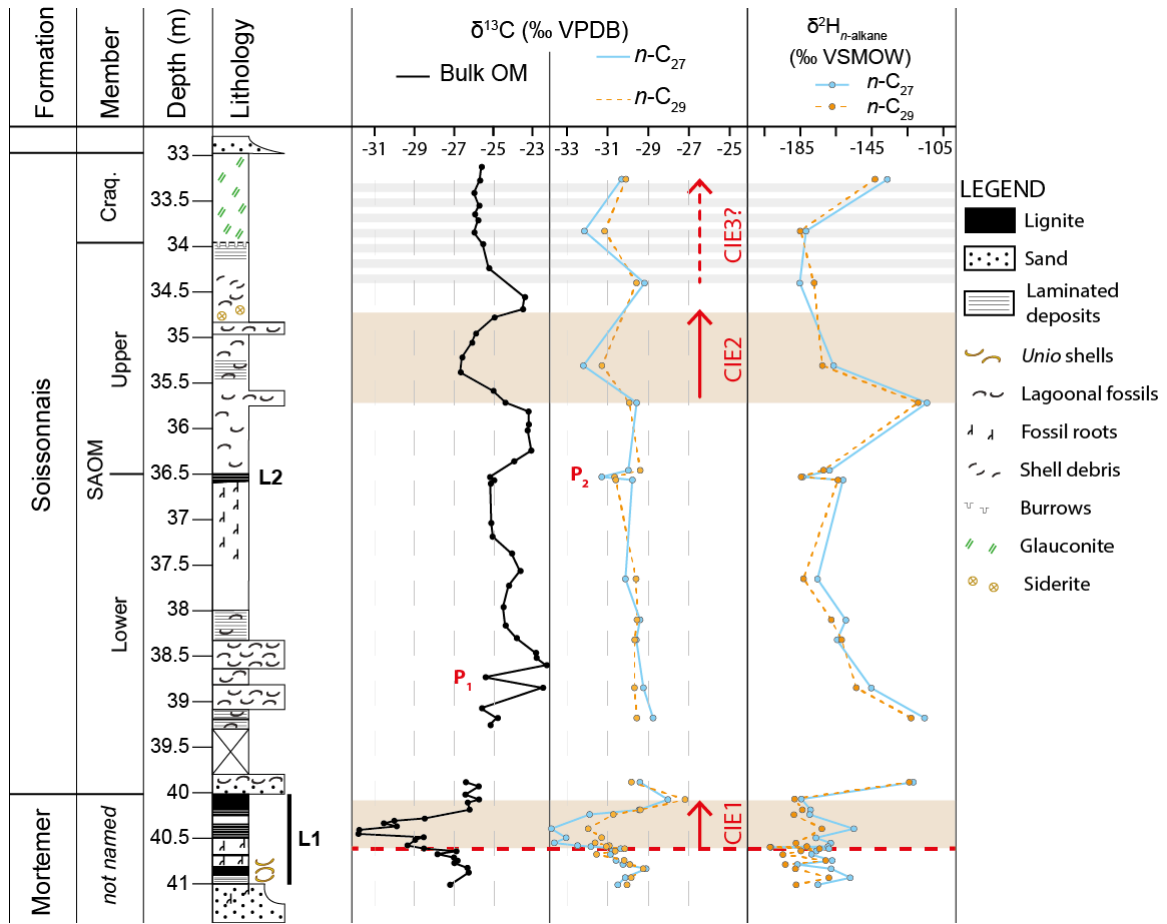
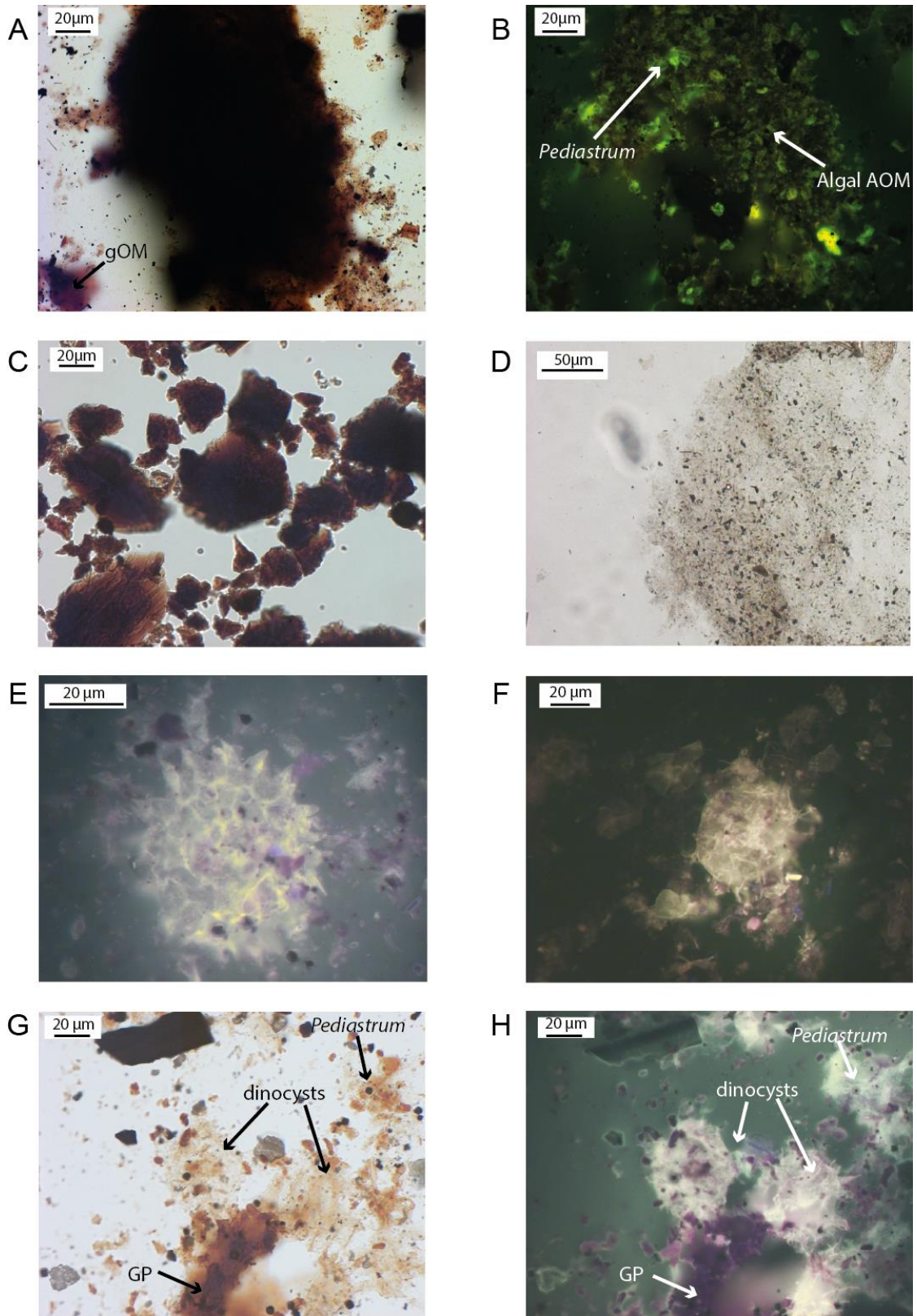


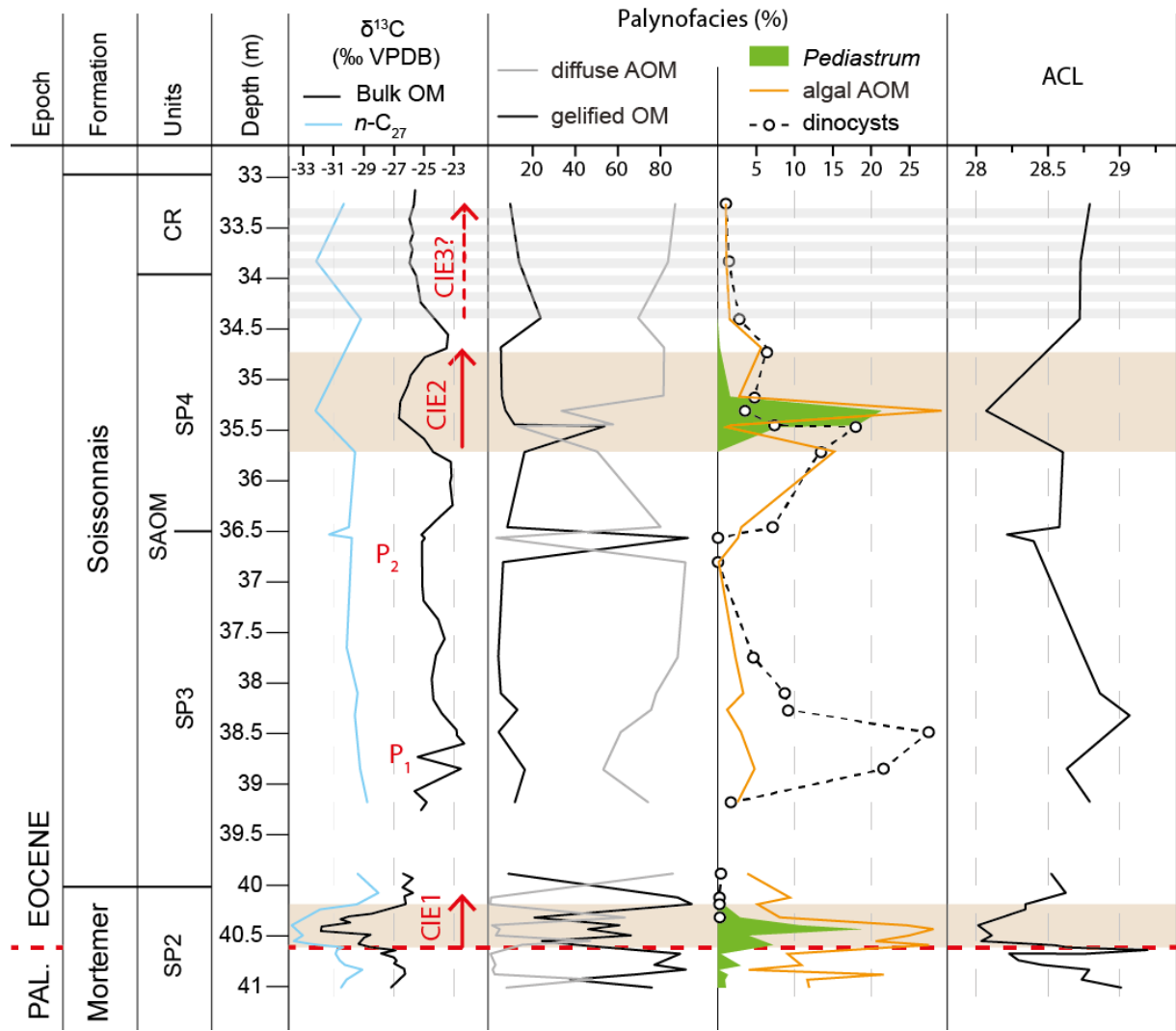
Figure 3



825

826

Figure 4



827

828

Figure 5





Sample Number	Lab. Sample	Weight molten (g)	K <sub>2</sub> O (wt.%)	<sup>40</sup> Ar* (%)	<sup>40</sup> Ar* (10 <sup>14</sup> at/g)	Age ± 2σ (Ma)
<b>GL-CRA (I)</b>	<b>lab 1658</b>	<b>0.02117</b>	<b>5.730</b>	<b>71.05</b>	<b>2.744</b>	<b>54.4 ± 0.8</b>
<b>GL-CRA (II)</b>	<b>lab 1659</b>	<b>0.02226</b>	<b>5.730</b>	<b>67.47</b>	<b>2.696</b>	<b>53.6 ± 0.8</b>
<b>GL92-A64 (I)</b>	<b>lab 1666</b>	<b>0.03230</b>	<b>6.630</b>	<b>81.75</b>	<b>3.095</b>	<b>53.1 ± 0.8</b>
<b>GL92-A64 (II)</b>	<b>lab 1672</b>	<b>0.02226</b>	<b>6.630</b>	<b>78.33</b>	<b>3.121</b>	<b>52.8 ± 0.7</b>

831

Table 1